The Cryosphere Discuss., 6, 3503–3538, 2012
www.the-cryosphere-discuss.net/6/3503/2012/
doi:10.5194/tcd-6-3503-2012

The Cryosphere Discussions

Satellite-Derived Volume Loss Rates and Glacier Speeds for the Cordillera Darwin Icefield, Chile

A. K. Melkonian[1], M. J. Willis[1], M. E. Pritchard[1], A. Rivera[2,3], F. Bown[2], and S. A. Bernstein[4]

[1]Department of Earth and Atmospheric Sciences, Cornell University, Ithaca, New York, USA
[2]Centro de Estudios Científicos (CECs), Valdivia, Chile
[3]Departamento de Geografía, Universidad de Chile, Santiago, Chile
[4]St. Timothy's School, 8400 Greenspring Ave, Stevenson, MD, 21153, USA

Received: 12 July 2012 – Accepted: 31 July 2012 – Published: 31 August 2012

Correspondence to: A. K. Melkonian (akm26@cornell.edu)

Published by Copernicus Publications on behalf of the European Geosciences Union.

Abstract

We produce the first icefield-wide volume change rate and glacier velocity estimates for the Cordillera Darwin Icefield (CDI), a 2605 km^2 temperate icefield in Southern Chile (69.6° W, 54.6° S). Velocities are measured from optical and radar imagery between 2001–2011. Thirty-seven digital elevation models (DEMs) from ASTER and the SRTM are stacked and a weighted linear regression is applied to elevations on a pixel-by-pixel basis to estimate volume change rates.

The CDI lost mass at an average rate of 3.9 ± 0.3 Gt yr^{-1} between 2000 and 2011, equivalent to a sea level rise (SLR) of 0.01 ± 0.001 mm yr^{-1}. Thinning is widespread, with concentrations near the front of two northern glaciers (Marinelli, Darwin) and one western (CDI-08) glacier. Thickening is apparent in the south, most notably over the advancing Garibaldi Glacier. We attribute this thinning pattern to warmer temperatures, particularly in the north, which triggered rapid retreat at Marinelli Glacier (~4 km from 2001–2011).

Velocities are obtained over many of the swiftly flowing glaciers for the first time. We provide a repeat speed timeseries at the Marinelli Glacier. Maximum front speeds there accelerated from 7.5 m day^{-1} in 2001 to 9.5 m day^{-1} in 2003, to a peak of 10 m day^{-1} in 2011.

1 Introduction

The Cordillera Darwin Icefield (CDI) is a small icefield, located in the southernmost Andes (Fig. 1) in Tierra del Fuego. The temperate icefield is coalesced around two main mountain peaks, Mount Darwin 2469 m a.s.l., (e.g., Koppes et al., 2009) and Mount Sarmiento 2300 m a.s.l., (e.g., Strelin et al., 2008) and covers 2605 km^2, measured from ice outlines derived from satellite imagery acquired from 2001 to 2004. It extends roughly 200 km west-to-east from 71.8° W to 68.5° W and roughly 50 km south-to-north from 54.9° S to 54.2° S. The icefield is bounded to the north by the Almirantazgo Ford

TCD
6, 3503–3538, 2012

and the Beagle Channel in the south. Precipitation during the winter comes predominantly from the south/southwest (Holmlund and Fuenzalida, 1995), and the E–W orientation of the CDI leads to an orographic effect with greater snowfall on southern glaciers and drier, warmer conditions on northern glaciers (Holmlund and Fuenzalida, 1995; Strelin and Iturraspe, 2007; Koppes et al., 2009).

There are few studies on the CDI compared to other temperate icefields (Masiokas et al., 2009; Lopez et al., 2010), such as the Alaskan icefields, the Northern Patagonian Icefield (NPI) and the Southern Patagonian Icefield (SPI) (e.g., Arendt et al., 2002; Rignot et al., 2003; Berthier et al., 2007, 2010; Glasser et al., 2011; Willis et al., 2012a). Climate and mass balance studies are scarce for southern hemisphere ice bodies outside of Antarctica (Holmlund and Fuenzalida, 1995; Lopez et al., 2010), due to the difficult access and weather. Here we focus on the third largest temperate icefield in the southern hemisphere (Bown et al., 2013), which along with the NPI and SPI, has experienced a rapid reduction in ice-covered area (Rivera et al., 2007; Masiokas et al., 2009; Lopez et al., 2010; Willis et al., 2012b).

The loss of ice at the CDI has been attributed to climatic changes in the region, including warming during the 20th century (Holmlund and Fuenzalida, 1995; Lopez et al., 2010) (from climate station data) in conjunction with decreased precipitation (Quintana, 2004). Since the mid-20th century, and despite a reduction in regional precipitation, the CDI in particular has experienced increased precipitation on its southern side (Strelin and Iturraspe, 2007), with decreased precipitation and warmer temperatures on its northern side inferred from NCEP-NCAR climate model results (Koppes et al., 2009).

Temperate icefields are disproportionately large contributors to SLR (e.g., Arendt et al., 2002; Rignot et al., 2003); Rignot et al., 2003 claim this is particularly true of the Patagonian glaciers, which they say account for 9 % of the non-polar contribution to SLR. The CDI, along with the NPI and SPI, provides an opportunity to examine the response of different glaciers (e.g. calving vs. non-calving) in different climates (maritime on the southern side versus more continental on the northern side) to regional changes in climate (Holmlund and Fuenzalida, 1995), and unlike the NPI and SPI the

TCD
6, 3503–3538, 2012

contribution of the CDI to SLR has not yet been estimated (Lopez et al., 2010). Finally, the CDI is the closest icefield to the Antarctic Peninsula, a region that has also experienced significant warming. Thinning and acceleration have been observed on glaciers in the Antarctic Peninsula and the NPI (Pritchard and Vaughan, 2007; Willis et al., 2012a), we assess whether this is the case for any glaciers on the CDI. Mass loss at the CDI might be contaminating GRACE measurements of nearby icefields (e.g. the NPI, SPI and Antarctic Peninsula), so our constraints on the mass loss rate occurring at the CDI will help isolate this signal.

In this study we calculate both the elevation change rates ($\frac{dh}{dt}$) over the entire CDI and measure glacier velocities using pixel-tracking applied to pairs of optical and radar images. With $\frac{dh}{dt}$ and an assumed ice density we can estimate the mass change rate and give a measurement of the CDI's contribution to SLR, allowing us to compare its SLR contribution to other icefields. We can also use the surface elevation change rates to identify which glaciers are providing the largest contribution to SLR and should be the focus of further study. Additionally, measuring glacier velocities allows an estimate of mass flux out of the glacier if the thickness is known. Our results will provide a baseline measurement over many glaciers and areas of the icefield for which ice velocities have not been measured.

2 Methods

2.1 Data preparation

The Advanced Spaceborne Thermal Emission and Reflection Radiometer (ASTER) has a stereo-imaging capability, enabling DEMs to be generated on-demand by NASA's Land Processes Distributed Active Archive Center (LP DAAC) (Fujisada et al., 2005). ASTER DEMs (product 14) are used to calculate $\frac{dh}{dt}$, while band 3N images (product 1B) are used for pixel-tracking. NASA's Automatic Registration and Orthorectification Package (AROP; Gao et al., 2009) is used to co-register ASTER images and DEMs to

TCD
6, 3503–3538, 2012

a Landsat GLS image (available from the Global Land Cover Facility) and orthorectify the ASTER L1B images using the Shuttle Radar Topography Mission (SRTM) DEM (acquired in 2000). Landsat GLS images are orthorectified to the SRTM DEM (Tucker et al., 2004), so co-registering the ASTER imagery to the Landsat GLS image effectively co-registers them to the SRTM DEM (see Melkonian, 2011 and Willis et al., 2012a for details).

2.2 Elevation change rates

Horizontally co-registered ASTER DEMs are vertically co-registered and a weighted linear regression is applied to calculate $\frac{dh}{dt}$ for each pixel. 36 ASTER DEMs (derived from imagery acquired from 2001 to 2011) and the SRTM DEM (acquired in February 2000) are processed, with an average of 4–5 elevations per pixel incorporated into the regression. Each elevation is weighted by the inverse of the standard deviation of the bedrock elevation differences between its ASTER DEM and the SRTM DEM. This is a common measure of the uncertainty associated with ASTER DEM elevations (Fujisada et al., 2005; Howat et al., 2008b). Horizontal misalignment will appear as off-ice ("bedrock") elevation differences when comparing ASTER DEMs to the SRTM DEM, and is therefore included. We typically find values from 8 m to 20 m as our uncertainty for ASTER DEMs, similar to other studies (Fujisada et al., 2005; San and Süzen, 2005; Rivera et al., 2007; Howat et al., 2008b; Berthier et al., 2010).

The first elevation in our timeseries is SRTM for 94 % of the pixels, for the remaining areas we use the first available elevation from ASTER. Below the Equilibrium Line Altitude (ELA), only elevations within +5/–30 m yr^{-1} of the first elevation in time are incorporated into the regression to avoid the influence of clouds and other erroneous elevations (Fig. 10). Above the ELA, only elevations within +5/–10 m yr^{-1} of the first elevation are allowed (less thinning is expected in the accumulation zone than in the ablation zone). We do not expect significant areas with thinning greater than 30 m yr^{-1}, the maximum coherent thinning that we observe is ~25 m yr^{-1} at the front of glaciers such as Marinelli that are known to be rapidly retreating (Fig. 10). Experimenting with

TCD
6, 3503–3538, 2012

different positive bounds, examination of plots such as those in Fig. 10 and consideration of maximum precipitation rates measured in Patagonia led us to select $+5\,\mathrm{m\,yr^{-1}}$ as our upper limit. Discontinuous and incoherent "splotches" of extreme positive $\frac{dh}{dt}$ appear when greater deviations from the first elevation are allowed (e.g. $+30\,\mathrm{m\,yr^{-1}}$). Additionally, measurements of precipitation in Patagonia nowhere show significant zones with greater than $\sim 10\,\mathrm{m\,yr^{-1}}$ of precipitation (e.g., Holmlund and Fuenzalida, 1995; Rignot et al., 2003; Rasmussen et al., 2007; Koppes et al., 2011). Given that not all precipitation is retained to contribute to longer-term thickening, $+5\,\mathrm{m\,yr^{-1}}$ is chosen as a reasonable upper limit on the maximum thickening expected over the large areas covered in this study (e.g. a point measurement may yield a $\frac{dh}{dt}$ higher than $+5\,\mathrm{m\,yr^{-1}}$ but we would not expect that to be reflective of sustained thickening rates over areas of square kilometers). The exception to our $+5\,\mathrm{m\,yr^{-1}}$ constraint is the lower ablation zone (<650 m elevation) of Garibaldi Glacier, which is known to be advancing (Fig. 7), where we allow $+10\,\mathrm{m\,yr^{-1}}$ to accommodate higher thickening rates.

In order to determine the ELA and distinguish where to impose our different constraints, we examine late season (January and February) ASTER images. We are able to use those to measure the ELA for 11 larger glaciers, for the rest of the icefield, we assume a regional ELA of 1090 m (Strelin and Iturraspe, 2007).

The volume change rate at each pixel is the $\frac{dh}{dt}$ for the pixel multiplied by the area of the pixel. Summing together the volume change rate of every pixel yields a volume change rate ($\frac{dV}{dt}$) for the entire icefield.

The uncertainty associated with the $\frac{dh}{dt}$ for each pixel is calculated from the model covariance matrix (e.g., Aster et al., 2005). The 95 % confidence interval for the volume change rate uncertainty is calculated using the formula: $1.96 \times \frac{U}{\sqrt{N}}$, where U is the "volume" of uncertainty (the sum of the uncertainty at each pixel multiplied by the pixel area) and N is the number of pixels (e.g., Howat et al., 2008b). We determine N by dividing the total area by the area over which off-ice $\frac{dh}{dt}$ are correlated (e.g., Rolstad et al., 2009). This is determined by finding the area at which the variance of the off-ice

TCD
6, 3503–3538, 2012

$\frac{dh}{dt}$ begins to "flatten" (see Rolstad et al., 2009 and Willis et al., 2012a for details on the method), which we estimate to be 1260 m by 1260 m (Fig. 9).

$\frac{dV}{dt}$ is multiplied by the density of glacier ice, set to 900 kg m^{-3} (e.g., Cuffey and Paterson, 2010) to produce an estimate of the mass change rate. Future ground-based measurements of densities on the CDI will be needed to find more accurate and precise values.

We have a sufficient number of ASTER DEMs to provide $\frac{dh}{dt}$ rates for 96 % of the total area of the icefield. Each pixel in the remaining small gaps is filled with the median $\frac{dh}{dt}$ value within 1 km. This is more accurate than using an elevation binning method or simply extrapolating an average rate. For example, the average low-elevation $\frac{dh}{dt}$ and overall average $\frac{dh}{dt}$ are both negative, these rates would not be suitable for filling a gap near the front of Garibaldi Glacier, which is known to be advancing and where we measure positive $\frac{dh}{dt}$ at low elevations.

We cannot directly measure changes in the sub-aqueous volume of ice, so we examine imagery of several glaciers that we know have advanced or retreated during the period covered by our study and use these to determine area change over water at the fronts of these glaciers. Once the area change is measured from available imagery, we assume an average depth below water of 150 m for Marinelli Glacier (see Koppes et al., 2009, Fig. 4a and b) and 60 m for the other glaciers, with an uncertainty of ± 50 m (the uncertainty on the change in area of each glacier is negligible). Dividing the sub-aqueous volume change by the time interval separating the images used to find area change gives the volume change rate. We add sub-aqueous volume change together for the glaciers we examine and combine that number with the overall mass loss rate derived from our $\frac{dh}{dt}$. This calculation is intended to show that sub-aqueous mass loss, while not well constrained in this study, is an order of magnitude lower than the overall mass change rate calculated from $\frac{dh}{dt}$.

Penetration of C-band radar into ice and (particularly) snow (e.g., Rignot et al., 2001) is a potential problem when using the SRTM DEM to estimate $\frac{dh}{dt}$. Willis et al. (2012b) compare X-band SRTM elevations (which should have negligible penetration)

TCD
6, 3503–3538, 2012

with C-band SRTM elevations and find approximately 2 m of C-band penetration over the SPI at all elevations. Due to a lack of X-band SRTM coverage over the CDI a similar analysis fails to provide any insight here, however, we perform our processing with 2 m added to every SRTM elevation, which increases our mass loss rate by about 13 %. The CDI is colder than the SPI, which could lead to less wet conditions and greater penetration (Rignot et al., 2001), however, as noted above, we do not have adequate X-band data to quantify the difference. This effect should be considered when discussing mass loss from the CDI until such time as future studies help resolve the issue of radar penetration into ice and snow, which varies considerably depending on local conditions (Gardelle et al., 2012).

2.3 Velocities

In this section we describe how we use data from three different satellites with different resolutions to measure sub-pixel offsets and convert them to glacier velocities.

2.3.1 ASTER

Sub-pixel offsets between ASTER image pairs (pixel resolution of 15 m/pixel) are measured via normalized amplitude cross-correlation, with a spatial resolution of 120 m (i.e., a step size between cross-correlations of 8 pixels, see Melkonian, 2011 and Willis et al., 2012a for details). This technique, known as "pixel-tracking", has been used to track velocities on many glaciers (e.g., Scambos et al., 1992; Stearns and Hamilton, 2005; Howat et al., 2008a; Willis et al., 2012a).

AROP is used to co-register the more recent scene in a pair of orthorectified ASTER images to the earlier scene to minimize misfits. The open source ROI_PAC's "ampcor" routine (Rosen et al., 2004) is used to calculate E–W and N-S offsets. The results are post-filtered by excluding offsets with a signal-to-noise ratio (SNR, which is the peak cross-correlation value divided by the average) below a manually-selected threshold (Melkonian, 2011). A linear elevation-dependent correction (determined from apparent

TCD
6, 3503–3538, 2012

"bedrock" velocities) is applied to the velocities to correct for the elevation-dependent bias due to imprecise co-registration/orthorectification (Nuth and Kääb, 2011) (Fig. 11). Co-registration errors lead to systematic elevation-dependent displacement errors over the ice surface (Ahn and Howat, 2011). Applying an elevation-dependent correction based on the displacement of off-ice areas largely removes this (Fig. 12).

Uncertainty for each pair is estimated from motion on ice-adjacent "bedrock" (see Willis et al., 2012a for details), which should be zero. Horizontal misalignment leads to off-ice motions when calculating offsets, so error due to misalignment is included in the uncertainty estimate.

2.3.2 QuickBird 2

A high-resolution (1 m/pixel) QB02 image pair from 2011 (07/30/2011-08/16/2011) is run through largely the same processing applied to ASTER image pairs to generate offsets at 30 m resolution. The images are orthorectified to a 2007 ASTER DEM with Rational Polynomial Coefficients (RPC's).

2.3.3 Advanced Land Observing Satellite (ALOS)

We use pixel-tracking to calculate velocities from two ascending ALOS pairs (09/28/2008–11/13/2008 and 01/04/2011-02/19/2011) with an initial pixel resolution of 3.3 m (azimuth) by 8.3 m (range). The offsets have an effective resolution of approximately 150 m (azimuth) by 200 m (range), based on the step size of 50 pixels (azimuth) by 25 pixels (range). The Synthetic Aperture RADAR (SAR) images cover a broader area than the optical images, providing velocities at many glaciers with no ASTER observations. SAR pixel-tracking also performs well in the snow-covered, high-altitude accumulation zone where optical images lack trackable features. The ALOS pairs fail to capture the high speeds near the fronts of several glaciers due to decorrelation caused by strain and possibly melting.

TCD
6, 3503–3538, 2012

Raw ALOS SAR data are processed using ROI_PAC and offsets are produced by "ampcor". The results are SNR-filtered and run through the elevation-dependent correction routine. ALOS interferometry does not yield velocities due to the relatively large motions, long separation between scenes, and changing surface characteristics.

2.3.4 Orthorectification errors from thinning

Pronounced thinning can cause orthorectification errors that do not show up in the off-ice velocities. The longer the timespan between the acquisition date of imagery used to measure offsets and the SRTM DEM (acquired in 2000), the greater the error. Examining our $\frac{dh}{dt}$ results (Fig. 1) reveals this to be a potential problem over the three most rapidly thinning glaciers: Marinelli, CDI-08 and Darwin. For Marinelli Glacier we mitigate this effect by orthorectifying QuickBird 2 imagery from 2011 to a 2007 ASTER DEM rather than the SRTM DEM. The two ASTER pairs for which we obtain Marinelli front speeds are from 2001 and 2003, closer to the acquisition date of the SRTM DEM. The vertical error for these pairs should not be too large - on the order of 20 to 60 m. The pair we use to obtain front velocities at Darwin Glacier is from 2001, again, close enough in time to the SRTM DEM to avoid significant errors. Velocities over CDI-08 are from radar pixel-tracking, where orthorectification is not an issue.

3 Results

3.1 Elevation change rates

A map of $\frac{dh}{dt}$ for the entire icefield is shown in Fig. 1. We find an area-averaged $\frac{dh}{dt}$ of $-1.6 \pm 0.1\,\mathrm{m\,yr^{-1}}$ of ice for the CDI and an overall $\frac{dV}{dt}$ of $-4.2 \pm 0.3\,\mathrm{km^3\,yr^{-1}}$, with thinning concentrated at lower elevations. Estimates of the sub-aqueous mass loss rate for four glaciers, Marinelli, CDI-08, Darwin and Garibaldi add -0.12 ± 0.06 $\mathrm{km^3\ yr^{-1}}$ to the overall $\frac{dV}{dt}$, giving a total $\frac{dV}{dt}$ of $-4.3 \pm 0.3\,\mathrm{km^3\,yr^{-1}}$, equivalent to a mass loss rate

TCD
6, 3503–3538, 2012

of $3.9 \pm 0.3\,\mathrm{Gt\,yr^{-1}}$. Most mass loss (76 %) occurs in the ablation zone (which covers 60 % of the icefield area). Significant thinning at Marinelli Glacier, Darwin Glacier, and CDI-08 Glacier accounts for $1.4 \pm 0.1\,\mathrm{km^3\,yr^{-1}}$ (31 %) of the icefield's volume loss.

Some thickening is occurring on the southern and south-facing areas of the icefield. This is most apparent at Garibaldi Glacier, where there are extensive positive $\frac{dh}{dt}$ throughout the ablation zone. This is consistent with Garibaldi's advance of ~1 km between 2003 and 2011 (Fig. 7). Table 1 gives the $\frac{dV}{dt}$ for the 16 largest glaciers, with rates for the entire basin, the accumulation zone and the ablation zone.

3.2 Velocities

Pixel-tracking is successfully applied to twenty ASTER image pairs, one QB02 pair and two ALOS pairs with acquisition dates between August 2001 and August 2011 (Fig. 8). ASTER pixel-tracking generally performs better on the northern half of the CDI as there is less cloud cover than to the south (Holmlund and Fuenzalida, 1995; Strelin and Iturraspe, 2007). Composite speed results are shown in Fig. 2, velocities for individual pairs over selected glaciers are shown in Fig. 3.

Average front speeds for the tidewater Marinelli Glacier $133\,\mathrm{km^2}$ – the largest glacier of the CDI, (e.g., Koppes et al., 2009) are obtained between 09/07/2001 and 09/25/2001 (18 days) and 09/06/2003–09/13/2003 (7 days) from optical image pairs acquired by ASTER. In order to capture recent rapid motions at the front, we process a 07/16/2011 to 08/30/2011 QB02 pair (Fig. 4).

The Marinelli Glacier retreated ~4 km between 2001 and 2011 (measured from ASTER and QB02 imagery). Speed at the front reaches a maximum of $\sim 7.5 \pm 0.2\,\mathrm{m\,day^{-1}}$ in 2001, accelerating to $\sim 9.5 \pm 0.6\,\mathrm{m\,day^{-1}}$ in 2003 and a peak of $\sim 10 \pm 0.3\,\mathrm{m\,day^{-1}}$ in 2011. Fig. 4 shows a map of the 2011 velocities from the QB02 pair, along with longitudinal speed profiles for several pairs that highlight the high front speed and acceleration of about 30 % from 2001 to 2011.

TCD
6, 3503–3538, 2012

Speeds at the front of the tidewater Darwin Glacier (46 km^2), one of three major contributors to thinning, reach a maximum average of $9.7 \pm 0.8\,m\,day^{-1}$ for the period 09/25/2001 to 10/02/2001. No repeat measurements of motion from ASTER pairs are available for the Darwin Glacier. CDI-08 (127 km^2), the furthest west and south of the three most rapidly-thinning glaciers, reaches speeds of $2.0 \pm 0.5\,m\,day^{-1}$ within 1 km of its 01/15/2011 front (01/04/2011 to 02/19/2011 ALOS pair), unfortunately repeat speeds are not available for this glacier.

4 Discussion

4.1 Elevation Change Rates

4.1.1 Impact of ELA

Given the considerable uncertainty and variability of the regional ELA, we investigate the impact of changing the regional ELA on the $\frac{dV}{dt}$ for the whole icefield. An ELA of about 650 m has been found at the glaciers on the western and southern sides of the CDI (Bown et al., 2013), we perform processing using this as the regional ELA instead of 1090 m. The lower ELA produces a mass loss rate of $3.4 \pm 0.2\,Gt\,yr^{-1}$, which is only 10 % less than the mass loss rate (not including sub-aqueous mass change) with the higher ELA, as mass loss is concentrated at low elevations. Examining the impact of lowering the ELA highlights this concentration, as the percentage area of the ablation zone drops to 26 % yet it still accounts for 51 % of the mass loss.

4.1.2 Impact of allowed deviation from first elevation

The deviation allowed from the first elevation has a much larger impact on the mass loss rate. Changing the positive deviation allowed from +5 to +10 $m\,yr^{-1}$ decreases the

TCD
6, 3503–3538, 2012

mass loss rate from 3.9 Gt yr^{-1} to 1.8 Gt yr^{-1}. The rate produced by allowing +10 m yr^{-1} is given as a rough minimum estimate of the mass loss rate.

The un-symmetric cutoff (+5 m yr^{-1} versus –10/–30 m yr^{-1}) does bias our results towards thinning. However, we argue that an un-symmetric cutoff is more physically justified than a symmetric cutoff for the reasons given below.

Rapid retreat has been independently observed at Marinelli Glacier (Holmlund and Fuenzalida, 1995; Koppes et al., 2009), from which we know that a large amount of thinning must be occurring. The maximum allowed negative deviation from the first elevation of –30 m yr^{-1} just captures the maximum thinning at Marinelli Glacier (see Fig. 10, point 4). Also, the –30 m yr^{-1} cutoff is only applied within the ablation zone, a –10 m yr^{-1} cutoff is used in the accumulation zone, limiting the influence of erroneous thinning rates on our $\frac{dV}{dt}$ estimate.

The sub-panels in Fig. 10 illustrate the problem of using a positive cutoff of (for example) +30 m yr^{-1}, which would lead to the inclusion of ASTER elevations that are obvious outliers. Furthermore, a cutoff of +30 m yr^{-1} would allow thickening of around 300 m over ten years, an unrealistic amount based on estimates of precipitation in this region (Koppes et al., 2009; Lopez et al., 2010). As noted previously, a deviation of +5 m yr^{-1} from the first elevation is a more reasonable constraint on longer-term thickening over large areas of the icefield.

We note that ASTER elevations in the accumulation zone are generally less reliable due to greater cloud and snow cover (lack of contrast). Errors due to clouds tend to be positive rather than negative. This is another consideration (in addition to evidence of greater thinning than thickening) that leads us to use a larger negative than positive cutoff.

There has been much recent discussion of the need for more accurate and precise measurements of year-to-year thickening in icefield accumulation zones, e.g., at the Satellite and Ice Conference recently held in Santiago, Chile, where the idea was put forward of using LIDAR to measure the retained snow in the accumulation zone at the end of each melt year over a period of several years. Additional information that would

TCD
6, 3503–3538, 2012

allow us to refine our $\frac{dh}{dt}$ cutoffs would be most welcome, for now, the cutoffs we use seem best given current knowledge of this region.

4.1.3 Individual glaciers

A longitudinal profile of elevation and thinning rates for Marinelli Glacier (Fig. 5) illustrates both terminus retreat and the dramatic thinning occurring at the glacier. Thinning extends from the terminus all the way up the glacier, and continues into the highest parts of the accumulation zone. The profile of the glacier surface remains convex as the glacier thins and retreats, indicating that basal stresses are relatively high and the front remains grounded (Koppes et al., 2009) as of 11/13/2007. We find an average rate of retreat of 0.4 km yr^{-1} between 2001 and 2011. Koppes et al. (2009) measure a significantly more rapid retreat rate of 1 km yr^{-1} during the late 1990's from satellite and aerial photography, but their average rate of ~0.3 km yr^{-1} from 1960 to 2005 is similar to our 2001–2011 rate.

Koppes et al. (2009) infer thinning at Marinelli Glacier from the retreat rate (with a higher retreat rate leading to a higher thinning estimate), and because they measure the retreat rate slowing down from 1997 to 2005 they estimate a drop in volume loss, from a peak of 0.7 km^3 yr^{-1} in 1997 to 0.2 km^3 yr^{-1} by 2005. In contrast, our $\frac{dh}{dt}$ measurements show that volume change at Marinelli is sustained at a rate of -0.7 ± 0.1 km^3 yr^{-1} (Table 1, Figs. 5 and 10), in line with the 1997 rate of Koppes et al. (2009). This illustrates the utility of direct measurement for determining a more accurate $\frac{dV}{dt}$.

The tidewater Darwin Glacier has a similar thinning profile to the Marinelli Glacier (Fig. 6), retreating ~2 km from 02/22/2000 to 01/15/2011. The 01/15/2011 profile is convex for Darwin Glacier, indicating that the front remains grounded (e.g., Benn and Evans, 1998; Koppes et al., 2009). The retreat and thinning at Darwin Glacier, as for Marinelli Glacier, is characteristic of other fast-moving temperate tidewater glaciers (Koppes et al., 2009).

TCD
6, 3503–3538, 2012

CDI-08, the third glacier with a strong thinning signal, is on the southern side of the icefield and faces west. This position and aspect favors increased snowfall in the prevailing climate. Given its location and facing, CDI-08 is anomalous in that almost 2 km of retreat has occurred and the glacier has thinned rapidly between 2001 and 2011.

Garibaldi Glacier, on the southern side of the icefield, with a southern aspect, by contrast, has significant areas of positive $\frac{dh}{dt}$ in its ablation zone. Our $\frac{dh}{dt}$ here are based on sparse temporal coverage, and there is only one ASTER image (09/13/2003) that covers the entire front of Garibaldi Glacier. Comparison of a WorldView-1 (optical) image from 09/27/2011 with a 09/13/2003 ASTER image shows that the glacier has advanced by more than 1 km between 2003 and 2011. This gives us confidence in the positive $\frac{dh}{dt}$ we observe for Garibaldi Glacier, despite the limited data. The overall picture for Garibaldi Glacier is consistent with its position on the southern side of the icefield, where precipitation has increased (Holmlund and Fuenzalida, 1995; Strelin and Iturraspe, 2007), and aspect (facing south). Our results indicate the possibility of surge-like behavior, or perhaps the advance stage of a tidewater-cycle glacier. Confirmation of our remote sensing observations comes from field reports in the austral summer of 2007, when the glacier was observed destroying trees and frequently calving (Masiokas et al., 2009).

4.2 Velocities

4.2.1 Marinelli glacier

The maintenance of relatively high speeds at the front of Marinelli Glacier between 2001 and 2011 can be attributed, in part, to the observed gradient in $\frac{dh}{dt}$. There is rapid thinning and retreat at the front, with slower thinning rates upstream. This imbalance maintains surface slope near the glacier front, keeping up the driving stress according to the equation $\sigma = \rho g h \sin(\alpha)$, where σ is the driving stress, ρ is the density, g is

TCD
6, 3503–3538, 2012

gravitational acceleration, h is thickness and α is the slope (e.g., Cuffey and Paterson, 2010, p. 295).

It is unusual that speeds at the 2011 front are as high or higher than 2001 and 2003, despite the significant decrease in front extent and 4 km of ice front retreat. With elevation and velocity we can make a rough calculation to estimate the flux by assuming an average glacier depth below water of 150 m (see Koppes et al., 2009, Fig. 4a and b). Flux is calculated using transects perpendicular to glacier flow and as close as possible to the front for velocities from 09/07/2001 to 09/25/2001, 09/06/2003 to 09/13/2003 and 07/30/2011 to 08/16/2011. We assume an average front wall height of 50 m from the SRTM DEM and a 2007 ASTER DEM (similar to the average of 40 m assumed by Koppes et al., 2009) and add 150 m for a total glacier thickness along our transects. Multiplying this average glacier thickness of 200 m by the perpendicular velocity along the front transect yields a flux. Our flux measurements are $0.7 \pm 0.2\,\mathrm{km^3\,yr^{-1}}$ for the 2001 pair, $1.0 \pm 0.3\,\mathrm{km^3\,yr^{-1}}$ for the 2003 pair and $0.4 \pm 0.1\,\mathrm{km^3\,yr^{-1}}$ for the 2011 pair. Flux is greatest in 2003 due to higher speeds than 2001 and a more extensive front than 2011.

Our measured speeds show a different trend from those inferred by Koppes et al. (2009) from the retreat rate (with lower retreat rate leading to lower inferred speed). Whereas they have Marinelli glacier slowing from a terminus ice speed of $8\,\mathrm{m\,day^{-1}}$ in 2001 (similar to our $7.5\,\mathrm{m\,day^{-1}}$ 2001 speed) to $5.5\,\mathrm{m\,day^{-1}}$ in 2003, we observe an acceleration to $9.5\,\mathrm{m\,day^{-1}}$ in 2003. This reduces their estimated flux from a maximum of $1.25\,\mathrm{km^3\,yr^{-1}}$ in 1997 to a "21st century" (2001 through 2005) flux of $0.4\,\mathrm{km^3\,yr^{-1}}$. In contrast, the acceleration we observe from 2001 to 2003 increases the flux and contributes to the rapid, sustained thinning we observe over the same time period, illustrating again the usefulness of direct measurements, which in this case paint a picture of high front speed and sustained thinning rather than lower speeds and thinning.

The rapid retreat noted in this study and covered elsewhere (e.g., Koppes et al., 2009; Warren and Aniya, 1999), coupled with the thinning we observe between 2000 and 2011, suggests that Marinelli Glacier is a tidewater-cycle glacier (TWG) in retreat

TCD
6, 3503–3538, 2012

phase (e.g., Post et al., 2011). Jorge Montt Glacier on the SPI is a somewhat analogous TWG on the SPI, with a grounded front, thinning occurring at approximately the same rate, and a rapidly receding terminus (Rivera et al., 2012; Willis et al., 2012b). Front recession has opened fjords at both Marinelli and Jorge Montt, and rapid retreat was initiated as each glacier receded into deeper water (Holmlund and Fuenzalida, 1995; Koppes et al., 2009; Rivera et al., 2012). At Marinelli the retreat is thought to have been initiated by thinning linked to climate changes (Koppes et al., 2009). The fact that 2011 speeds at Marinelli are as high or higher than 2001 and 2003 suggests that the glacier has not yet retreated to fjord depths shallow enough to slow it down, and would lead us to expect further retreat until shallower depths are reached. Though there is significant variability from glacier to glacier on the Patagonian icefields (Rivera et al., 2012) the similar behavior of these two glaciers in the same region but on different icefields suggests that changing climate plays a role in retreat and thinning at Jorge Montt as well, given that the retreat was inferred to have been triggered by warming-induced thinning at the fronts of both glaciers.

Seasonal changes in conditions at Marinelli Glacier could be influencing our results, we note that the two ASTER pairs from which we obtain front speeds are both from September However, it is possible that the speeds in September 2001 and 2003 are different due to inter-annual variations in the onset of conditions affecting the glacier.

The 2011 QuickBird 2 pair is from 07/30/2011 to 08/16/2011. While this is not an entirely different season from the ASTER pairs, it is a month earlier, which is long enough for seasonal variations to possibly play a role in any observed speed differences. We consider it unlikely, however, that a seasonal component of motion is dominant in the 30 % increase in the front speed at Marinelli between September 2001 ($7.5\,\mathrm{m\,day^{-1}}$) and August 2011 ($10\,\mathrm{m\,day^{-1}}$). Unfortunately, we do not have enough repeat measurements to quantify any seasonal effect on speeds, especially given that our ALOS results over Marinelli from the austral summer do not reach the front.

TCD
6, 3503–3538, 2012

4.2.2 Other CDI Glaciers

Based on the $\frac{dh}{dt}$ results for Darwin Glacier, which have the same general pattern of thinning, we predict sustained, high front speeds similar to those observed at Marinelli Glacier. ALOS velocities show CDI-08 also speeds up towards its front (typical of tidewater glaciers) and is slower than either the Marinelli or Darwin Glacier, but there are no earlier speeds available to see what impact thinning there has had. Many of the non-tidewater terminating CDI glaciers slow down towards their fronts (e.g. Roncagli, Fig. 3c). The different thicknesses, bedrock topography and surface slopes of the glaciers on the CDI contribute to the variety of dynamic regimes observed.

5 Conclusions

Rapid thinning at three outlet glaciers on the CDI: Marinelli Glacier, Darwin Glacier, and CDI-08 Glacier, accounts for 31 % of the total volume loss rate (~1.4 out of 4.3 $km^3\ yr^{-1}$). Elevation profiles and optical imagery indicate that while Marinelli Glacier and Darwin Glacier have undergone significant retreat, they remain grounded at their fronts. Climate records from the 1940's through the 1990's show a warming trend in this region, which leads to higher temperatures along with decreased precipitation on the northern side of the icefield and an increase in precipitation on the southern side (Holmlund and Fuenzalida, 1995; Strelin and Iturraspe, 2007). Locally calibrated climate model results indicate a trend of warming and decreased snow input for Marinelli Glacier from the 1950's to 2009 (Koppes et al., 2009). These conditions have led to consistently negative mass balance on northern glaciers such as Marinelli throughout much of the 20th century, initiating thinning that caused the rapid retreat observed here and in several previous studies (Holmlund and Fuenzalida, 1995; Strelin and Iturraspe, 2007; Koppes et al., 2009). While the northern side is thinning, thickening is observed on individual southern and western glaciers, most notably Garibaldi Glacier, where measurements of positive $\frac{dh}{dt}$ are in keeping with its continued advance.

TCD
6, 3503–3538, 2012

Our limited repeat glacier speed measurements are consistent with our $\frac{dh}{dt}$ observations. The maximum front speed of Marinelli Glacier goes up by about 30 % as the front retreats between 2001 and 2011, with most of our measured acceleration occurring between 2001 and 2003. We would expect to observe the same pattern of sustained or accelerating front speeds at Darwin and CDI-08 Glacier (due to the ongoing retreat at these glaciers), but lack the requisite repeat measurements.

As is the case for the NPI and SPI, the CDI is losing mass relatively rapidly. The NPI covers an area of approximately 4000 km^2 and has an average $\frac{dh}{dt}$ of $-1.1 \pm 0.1\,\mathrm{m\,yr^{-1}}$ (Willis et al., 2012b), less than the CDI ($-1.7 \pm 0.1\,\mathrm{m\,yr^{-1}}$). The SPI covers 12,596 km^2 (Casassa et al., 2013) and has an average $\frac{dh}{dt}$ of $-1.8 \pm 0.1\,\mathrm{m\,yr^{-1}}$ (Willis et al., 2012b), very close the CDI rate. The average $\frac{dh}{dt}$ for CDI, however, is significantly more negative than the Juneau Icefield in Alaska (~4000 km^2), which has an average $\frac{dh}{dt}$ of $-0.09 \pm 0.03\,\mathrm{m\,yr^{-1}}$ (Melkonian, 2011).

Acknowledgements. ASTER data was provided by the LPDAAC. We thank the Alaska Satellite Facility (ASF) and the Japan Aerospace Exploration Agency (JAXA) for the ALOS data. Supported by NASA grant NNX08AI87G issued through the Science Mission Directorates Earth Science Division. Andrés Rivera and Francisca Bown acknowledge the GLIMS project for providing free satellite imagery in the full glacier inventory and surface variations coming in a separate book chapter. QuickBird 2 and WorldView 1 images provided by NGA Commercial Imagery Program. Sasha A. Bernstein was partially supported by the Cornell Rawlings Presidential Research Scholars Program.

TCD
6, 3503–3538, 2012

References

Ahn, Y. and Howat, I. M.: Efficient Automated Glacier Surface Velocity Measurement From Repeat Images Using Multi-Image/Multichip and Null Exclusion Feature Tracking, 49, 2838–2846, 2011. 3511

Arendt, A. A., Echelmeyer, K. A., Harrison, W. D., Lingle, C. S., and Valentine, V. B.: Rapid wastage of Alaska glaciers and their contribution to rising sea level., Science (New York, N.Y.), 297, 382–6, doi:10.1126/science.1072497, 2002. 3505

Aster, R. C., Borchers, B., and Thurber, C. H.: Parameter Estimation and Inverse Problems, Elsevier Inc., Burlington, MA, 2005. 3508

Benn, D. I. and Evans, D. J.: Glaciers & Glaciology, Oxford University Press Inc., New York, 1998. 3516

Berthier, E., Arnaud, Y., Kumar, R., Ahmad, S., Wagnon, P., and Chevallier, P.: Remote sensing estimates of glacier mass balances in the Himachal Pradesh (Western Himalaya, India), Remote Sensing of Environment, 108, 327–338, doi:10.1016/j.rse.2006.11.017, 2007. 3505

Berthier, E., Schiefer, E., Clarke, G. K. C., Menounos, B., and Rémy, F.: Contribution of Alaskan glaciers to sea-level rise derived from satellite imagery, Nat. Geosci., 3, 92–95, doi:10.1038/ngeo737, 2010. 3505, 3507

Bown, F., Rivera, A., Zenteno, P., Bravo, C., and Cawkwell, F.: First glacier inventory and recent glacier variations of Isla Grande de Tierra del Fuego and adjacent islands in Southern Chile, in: Global Land Ice Measurements from Space, edited by: Kargel, J. S., Leonard, G. J., Bishop, M. P., Kääb, A., and Raup, B., Praxis-Springer (Publishers), Heidelberg, ISBN: 978-3-540-79817-0, 2013. 3505, 3514

Casassa, G., Rodríguez, J. L., Rivera, A., and Bown, F.: A new glacier inventory for the Southern Patagonia Icefield and areal changes 1986–2000, in: Global Land Ice Measurements from Space, edited by: Kargel, J. S., Leonard, G. J.,Bishop, M. P., Kääb, A., and Raup, B., Praxis-Springer (Publishers), Heidelberg, ISBN: 978-3-540-79817-0, 2013. 3521

Cuffey, K. M. and Paterson, W. S. B.: The Physics of Glaciers, Butterworth-Heinemann, 4 Edn., 2010. 3509, 3518

Fujisada, H., Bailey, G., Kelly, G., Hara, S., and Abrams, M.: ASTER DEM performance, IEEE T. Geosci. Remote, 43, 2707–2714, doi:10.1109/TGRS.2005.847924, 2005. 3506, 3507

TCD
6, 3503–3538, 2012

Gao, F., Masek, J., and Wolfe, R. E.: Automated registration and orthorectification package for Landsat and Landsat-like data processing, J. Appl. Remote Sens., 3, 033515, doi:10.1117/1.3104620, 2009. 3506

Gardelle, J., Berthier, E., and Arnaud, Y.: Impact of resolution and radar penetration on glacier elevation changes computed from DEM differencing, J. Glaciol., 58, 419–422, doi:10.3189/2012JoG11J175, 2012. 3510

Glasser, N. F., Harrison, S., Jansson, K. N., Anderson, K., and Cowley, A.: Global sea-level contribution from the Patagonian Icefields since the Little Ice Age maximum, Nat. Geosci., 1–5, doi:10.1038/ngeo1122, 2011. 3505

Holmlund, P. and Fuenzalida, H.: Anomalous glacier responses to 20th century climatic changes in Darwin Cordillera, southern Chile, J. Glaciol., 41, 465–473, 1995. 3505, 3508, 3513, 3515, 3517, 3519, 3520

Howat, I. M., Joughin, I., Fahnestock, M., Smith, B. E., and Scambos, T. A.: Synchronous retreat and acceleration of southeast Greenland outlet glaciers 2000-06: ice dynamics and coupling to climate, J. Glaciol., 54, 646–660, doi:10.3189/002214308786570908, 2008a. 3510

Howat, I. M., Smith, B. E., Joughin, I., and Scambos, T. A.: Rates of southeast Greenland ice volume loss from combined ICESat and ASTER observations, Geophys. Res. Lett., 35, 1–5, doi:10.1029/2008GL034496, 2008b. 3507, 3508

Koppes, M., Hallet, B., and Anderson, J.: Synchronous acceleration of ice loss and glacial erosion, Glaciar Marinelli, Chilean Tierra del Fuego, J. Glaciol., 55, 207–220, doi:10.3189/002214309788608796, 2009. 3504, 3505, 3509, 3513, 3515, 3516, 3518, 3519, 3520

Koppes, M., Conway, H., Rasmussen, L. A., and Chernos, M.: Deriving mass balance and calving variations from reanalysis data and sparse observations, Glaciar San Rafael, northern Patagonia, 1950–2005, The Cryosphere, 5, 791–808, doi:10.5194/tc-5-791-2011, 2011. 3508

Lopez, P., Chevallier, P., Favier, V., Pouyaud, B., Ordenes, F., and Oerlemans, J.: A regional view of fluctuations in glacier length in southern South America, Glob. Planet. Change, 71, 85–108, doi:10.1016/j.gloplacha.2009.12.009, 2010. 3505, 3506, 3515

Masiokas, M. H., Rivera, A., Espizua, L. E., Villalba, R., Delgado, S., and Aravena, J. C.: Glacier fluctuations in extratropical South America during the past 1000 years, Palaeogeogr. Palaeoclim., 281, 242–268, doi:10.1016/j.palaeo.2009.08.006, 2009. 3505, 3517

TCD
6, 3503–3538, 2012

Melkonian, A. K.: Measuring Glacier Velocities and Elevation Change Rates from ASTER Data for the Juneau Icefield, Alaska, M.s. thesis, Cornell University, 2011. 3507, 3510, 3521
Nuth, C. and Kääb, A.: Co-registration and bias corrections of satellite elevation data sets for quantifying glacier thickness change, The Cryosphere, 5, 271–290, doi:10.5194/tc-5-271-2011, 2011. 3511
Post, A., O'Neel, S., Motyka, R. J., and Streveler, G.: A Complex Relationship Between Calving Glaciers and Climate, EOS Transactions, Am. Geophys. Union, 92, 2011. 3519
Pritchard, H. D. and Vaughan, D. G.: Widespread acceleration of tidewater glaciers on the Antarctic Peninsula, J. Geophys. Res., 112, 1–10, doi:10.1029/2006JF000597, 2007. 3506
Quintana, J.: Estudio de los factores que explican la variabilidad de la precipitación en Chile en escalas de tiempo interdecadal, Msc thesis, Universidad de Chile, 2004. 3505
Rasmussen, L. A., Conway, H., and Raymond, C. F.: Influence of upper air conditions on the Patagonia Icefields, Glob. Planet. Change, 59, 203–216, doi:10.1016/j.gloplacha.2006.11.025, 2007. 3508
Rignot, E., Echelmeyer, K., and Krabill, W.: Penetration depth of interferometric synthetic-aperture radar signals in snow and ice, Geophys. Res. Lett., 28, 3501–3504, doi:10.1029/2000GL012484, 2001. 3509, 3510
Rignot, E., Rivera, A., and Casassa, G.: Contribution of the Patagonia Icefields of South America to sea level rise., Science (New York, N.Y.), 302, 434–7, doi:10.1126/science.1087393, 2003. 3505, 3508
Rivera, A., Benham, T., Casassa, G., Bamber, J., and Dowdeswell, J.: Ice elevation and areal changes of glaciers from the Northern Patagonia Icefield, Chile, Glob. Planet. Change, 59, 126–137, doi:10.1016/j.gloplacha.2006.11.037, 2007. 3505, 3507
Rivera, A., Koppes, M., Bravo, C., and Aravena, J. C.: Little Ice Age advance and retreat of Glaciar Jorge Montt, Chilean Patagonia, Climate of the Past, 8, 1–12, doi:10.5194/cp-8-1-2012, 2012. 3519
Rolstad, C., Haug, T., and Denby, B.: Spatially integrated geodetic glacier mass balance and its uncertainty based on geostatistical analysis: application to the western Svartisen ice cap, Norway, J. Glaciol., 55, 666–680, doi:10.3189/002214309789470950, 2009. 3508, 3509
Rosen, P. A., Henley, S., Peltzer, G., and Simons, M.: Updated Repeat Orbit Interferometry Package, EOS, Trans. Am. Geophys. Union, 85, 47, doi:10.1029/2004EO050004, 2004. 3510

TCD
6, 3503–3538, 2012

San, B. T. and Süzen, M. L.: Digital elevation model (DEM) generation and accuracy assessment from ASTER stereo data, Int. J. Remote Sens., 26, 5013–5027, doi:10.1080/01431160500177620, 2005. 3507

Scambos, T. A., Dutkiewicz, M. J., Wilson, J. C., and Bindschadler, R. A.: Application of Image Cross-Correlation to the Measurement of Glacier Velocity Using Satellite Image Data, Remote Sens. Environ., 42, 177–186, 1992. 3510

Stearns, L. and Hamilton, G.: A new velocity map for Byrd Glacier, East Antarctica, from sequential ASTER satellite imagery, Ann. Glaciol., 41, 71–76, doi:10.3189/172756405781813393, 2005. 3510

Strelin, J. and Iturraspe, R.: Recent evolution and mass balance of Cordón Martial glaciers, Cordillera Fueguina Oriental, Glob. Planet. Change, 59, 17–26, doi:10.1016/j.gloplacha.2006.11.019,2007. 3505, 3508, 3513, 3517, 3520

Strelin, J., Casassa, G., Rosqvist, G., and Holmlund, P.: Holocene glaciations in the Ema Glacier valley, Monte Sarmiento Massif, Tierra del Fuego, Palaeogeogr. Palaeoclim., 260, 299–314, doi:10.1016/j.palaeo.2007.12.002, 2008. 3504

Tucker, C. J., Grant, D. M., and Dykstra, J. D.: NASAs Global Orthorectified Landsat Data Set, Photogr. Eng. Rem. Sens., 70, 313–322, 2004. 3507

Warren, C. R. and Aniya, M.: The calving glaciers of southern South America, Glob. Planet. Change, 22, 59–77, 1999. 3518

Willis, M. J., Melkonian, A. K., Pritchard, M. E., and Ramage, J. M.: Ice Loss Rates at the Northern Patagonian Icefield Derived Using a Decade of Satellite Remote Sensing, Remote Sens. Environ., doi:10.1016/j.rse.2011.09.017, 2012a. 3505, 3506, 3507, 3509, 3510, 3511

Willis, M. J., Melkonian, A. K., Pritchard, M. E., and Rivera, A.: Ice Loss from the Southern Patagonian Icefield, South America, between 2000 and 2012, Geophys. Res. Lett., 2012b. 3505, 3509, 3519, 3521

TCD
6, 3503–3538, 2012

Table 1. Volume Change Rates for the 16 Largest Outlet Glaciers on the CDI (includes estimates of sub-aqueous volume change for Marinelli, CDI-08, Garibaldi and Darwin).

Glacier	Area (km^2)	$\frac{dV}{dt}$ ($km^3\ yr^{-1}$)	Uncertainty ($km^3\ yr^{-1}$)	Ablation Area (km^2)	$\frac{dV}{dt}$ ($km^3\ yr^{-1}$)	Uncertainty ($km^3\ yr^{-1}$)	Accumulation Area (km^2)	$\frac{dV}{dt}$ ($km^3\ yr^{-1}$)	Uncertainty ($km^3\ yr^{-1}$)
Marinelli Glacier	132.93	–0.74	0.08	81.45	–0.68	0.07	51.48	–0.06	0.03
CDI-08 Glacier	127.42	–0.43	0.05	36.45	–0.26	0.03	90.97	–0.16	0.04
Roncagli Glacier	116.06	–0.18	0.07	42.23	–0.12	0.04	73.83	–0.06	0.05
Stoppani Glacier	102.04	–0.2	0.05	39.02	–0.12	0.04	63.03	–0.08	0.03
Garibaldi Glacier	63.86	0.02	0.07	21.01	0.04	0.05	42.85	–0.03	0.05
CDI_157 Glacier	57.42	–0.11	0.04	49.9	-0.09	0.03	7.52	–0.02	0.02
de_la_Vedova Glacier	56.83	–0.15	0.03	21.59	–0.07	0.02	35.24	–0.08	0.03
Bahia_Broken Glacier	53.22	–0.1	0.04	12.12	–0.04	0.02	41.1	–0.07	0.03
CDI_150 Glacier	52.31	–0.02	0.03	18.1	–0.0	0.02	34.21	–0.01	0.03
CDI_456 Glacier	51.22	–0.03	0.04	19.84	–0.02	0.02	31.39	–0.0	0.04
Darwin Glacier	45.61	–0.18	0.03	16.99	–0.14	0.02	28.62	–0.05	0.02
Cuevas Glacier	45.27	–0.06	0.04	4.58	–0.01	0.01	40.69	–0.05	0.04
CDI_455 Glacier	37.73	0.02	0.04	7.53	0.01	0.01	30.2	0.01	0.04
Oblicuo Glacier	29.81	0.02	0.05	19.38	0.01	0.04	10.43	0.01	0.02
CDI_48 Glacier	28.58	–0.04	0.02	20.68	–0.03	0.02	7.9	–0.01	0.01
CDI_142 Glacier	26.79	–0.05	0.04	12.55	–0.02	0.02	14.24	–0.03	0.03

TCD
6, 3503–3538, 2012

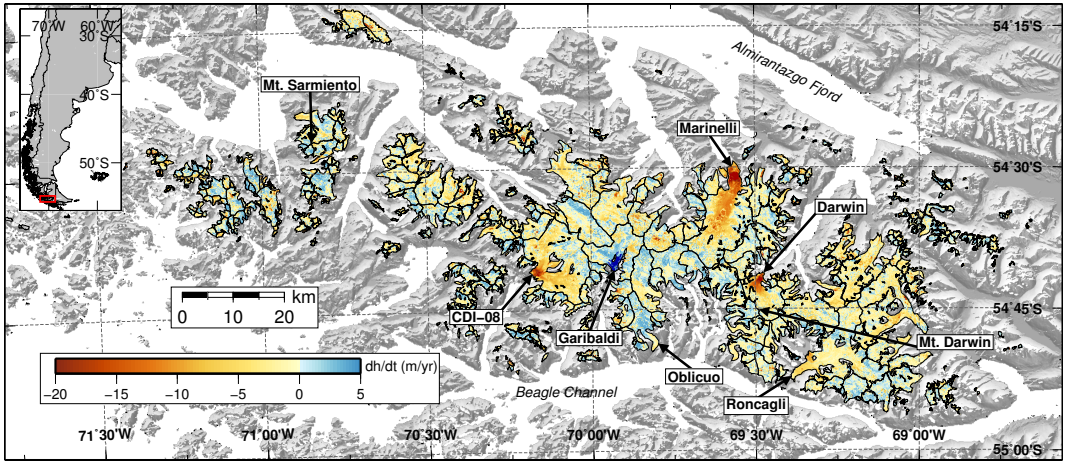

Fig. 1. Map of $\frac{dh}{dt}$ for the CDI (area indicated by red box in inset). Three glaciers, Marinelli, Darwin, and CDI-08, stand out with extensive thinning towards their fronts.

TCD
6, 3503–3538, 2012

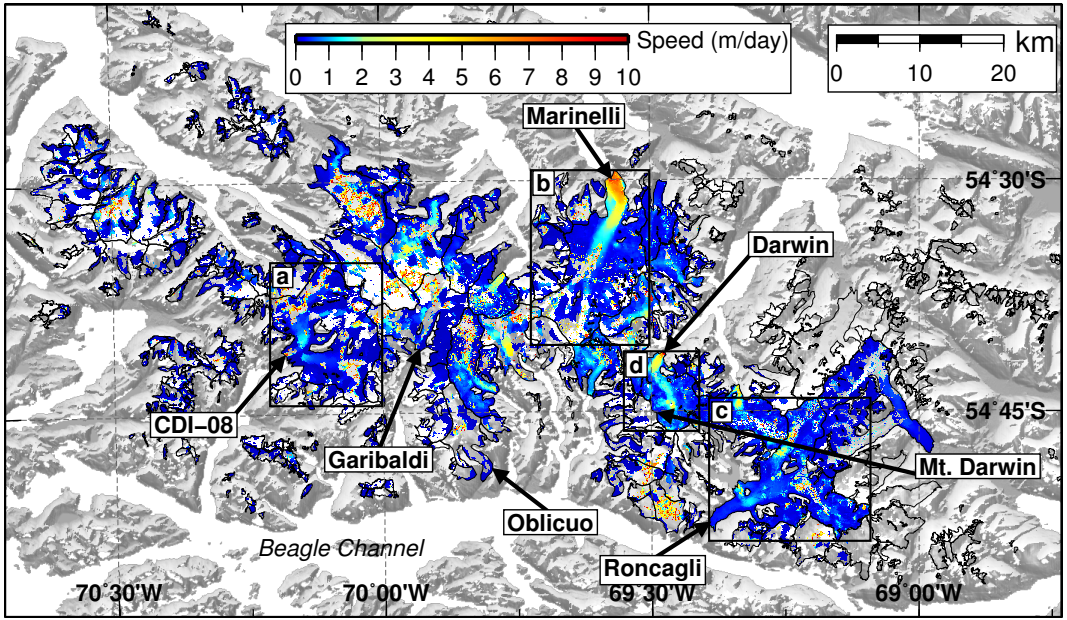

Fig. 2. Composite speed map for the CDI, incorporating ASTER- and ALOS-derived ice velocities.

TCD
6, 3503–3538, 2012

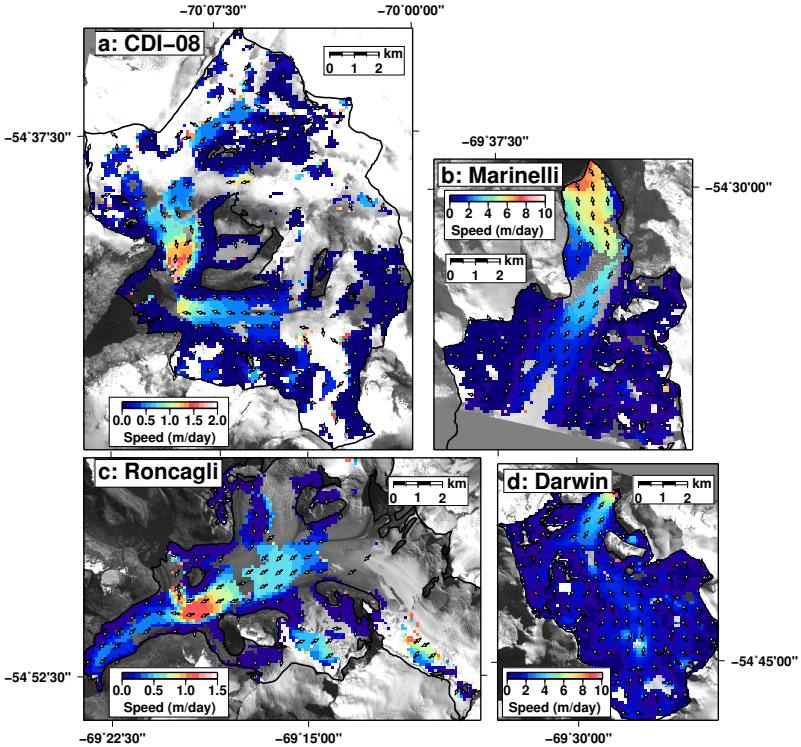

Fig. 3. Velocity maps for individual glaciers (separate color scale for each map), highlighting the quality of the velocity results for individual image pairs. **(a)** shows velocities from the 01/04/2011–02/19/2011 ALOS pair for CDI-08 Glacier with an ASTER image from 01/15/2011 in the background. **(b)** shows velocities from the 08/07/2001–09/25/2001 ASTER pair for Marinelli Glacier with an ASTER image from 09/07/2001 in the background. **(c)** shows velocities from the 01/04/2011–02/19/2011 ALOS pair for Roncagli Glacier with an ASTER image from 02/07/2002 in the background. **(d)** shows velocities from the 09/25/2001–10/02/2001 ASTER pair for Darwin Glacier with an ASTER image from 09/25/2001 in the background.

TCD
6, 3503–3538, 2012

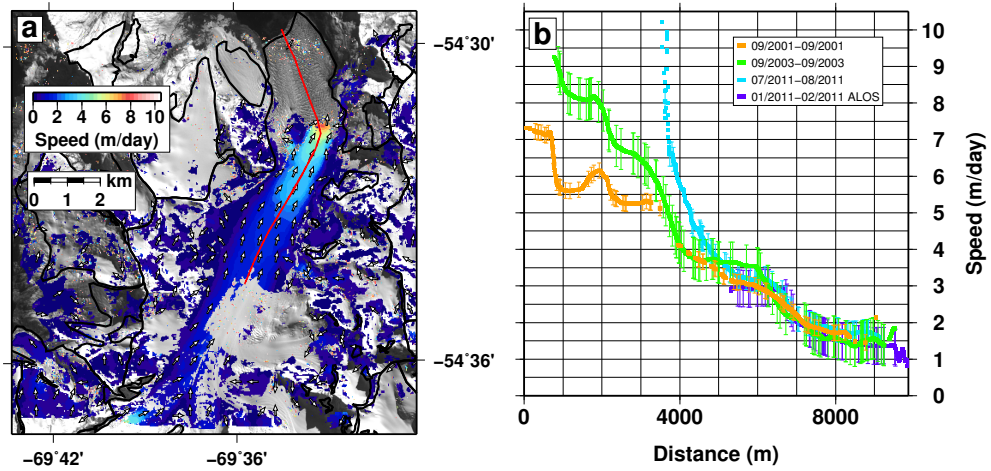

Fig. 4. Speeds for Marinelli Glacier. Panel **(a)** is a map of velocities from the QB02 (07/30/2011–08/16/2011) pair (background is the 09/07/2001 ASTER V3N image). Panel **(b)** shows profiles (indicated by the red line in panel **(a)** from two ASTER pairs (09/07/2001–09/25/2001, 09/06/2003–09/13/2003), the QB02 pair and an ALOS pair (01/04/2011–02/19/2011). The QB02 velocities extend to the 2011 front, comparing them with the 2001 ASTER V3N image and the ASTER speed profiles highlights the ∼4 km of front retreat between 2001 and 2011. Marinelli Glacier accelerates at its front from a maximum of $7.5 \pm 0.2\,\mathrm{m\,day^{-1}}$ in 2001, to $9.5 \pm 0.6\,\mathrm{m\,day^{-1}}$ in 2003 to a peak of $\sim 10 \pm 0.3\,\mathrm{m\,day^{-1}}$ in 2011. While the maximum speed from 2003 to 2011 does not change significantly, the speed profiles show a clear acceleration between 2003 to 2011 from the 2011 front to a distance of 5000 m on the profile.

TCD
6, 3503–3538, 2012

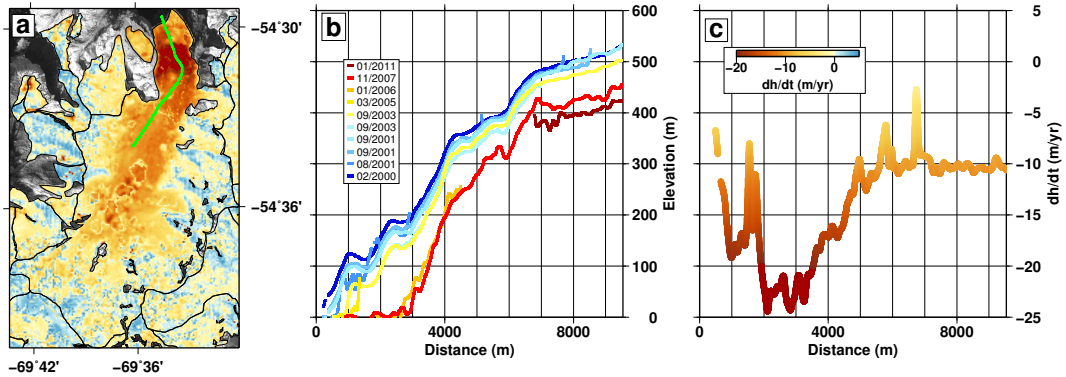

Fig. 5. $\frac{dh}{dt}$ and elevations for a longitudinal profile (starting towards the front) on Marinelli Glacier. A map of $\frac{dh}{dt}$ is shown in panel **(a)**, the track used in panels **(b)** and **(c)** is plotted in green. Panel **(b)** gives elevation profiles for different dates along the green track in **(a)**. The colorscale for the elevation profiles indicates the relative time of acquisition. Dark blue is the SRTM elevation (02/22/2000), the red track extending to the front is an ASTER DEM from 11/13/2007. From the elevation profiles it is clear that the front has retreated between 2–3 km between 2000 and 2007. Panel **(c)** shows the $\frac{dh}{dt}$ profile for the green track in **(a)**. The colorscale for panel **(a)** is the same as panel '**(c)**.

TCD
6, 3503–3538, 2012

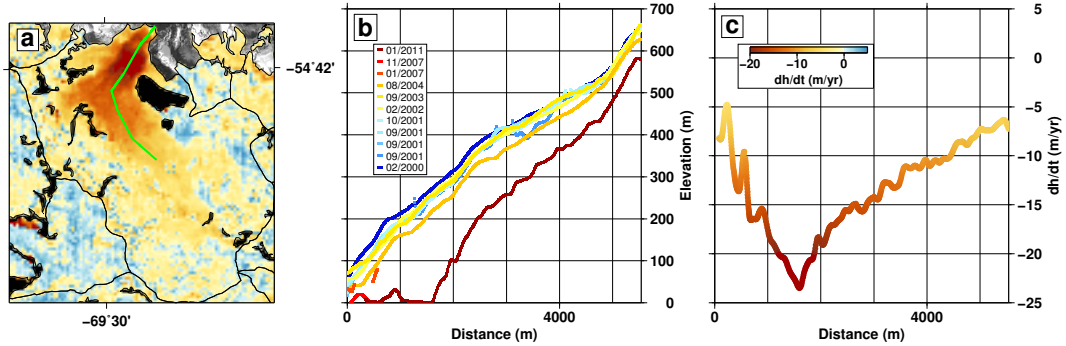

Fig. 6. $\frac{dh}{dt}$ and elevations for a longitudinal profile (starting towards the front) on Darwin Glacier. A map of $\frac{dh}{dt}$ is shown in panel **(a)**, the track used in panels **(b)** and **(c)** is plotted in green. Panel **(b)** gives elevation profiles for different dates along the green track in **(a)**. The colorscale for the elevation profiles indicates the relative time of acquisition. Dark blue is the SRTM elevation (02/22/2000), the red track extending to the front is an ASTER DEM from 01/15/2011. Panel **(c)** shows the $\frac{dh}{dt}$ profile for the green track in **(a)**. The colorscale for panel **(a)** is the same as panel **(c)**.

TCD
6, 3503–3538, 2012

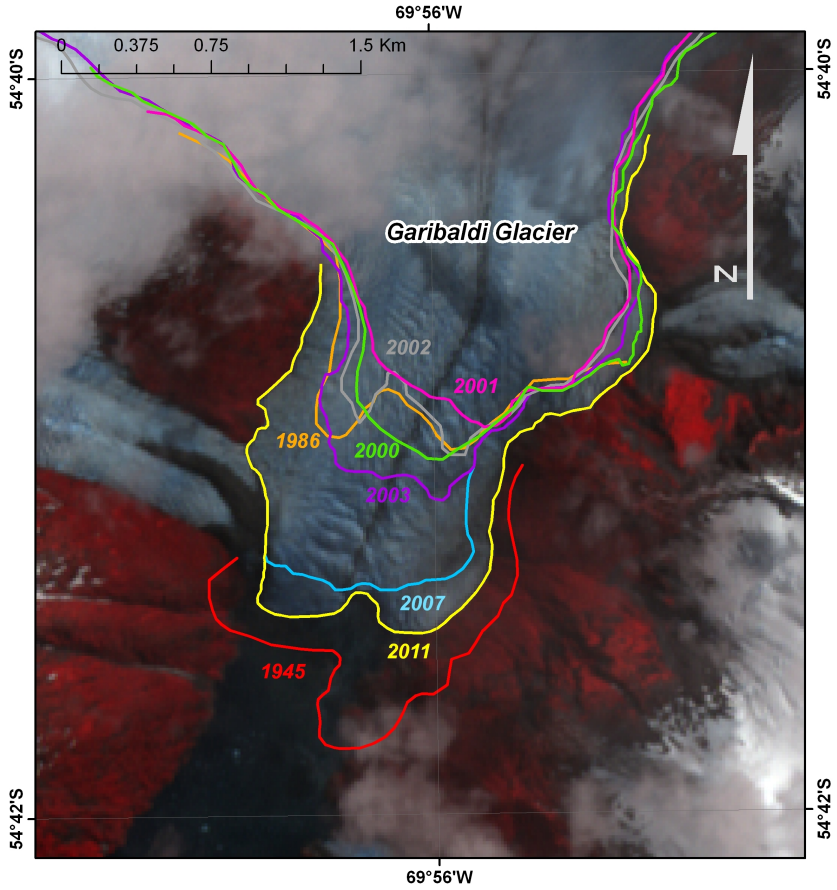

Fig. 7. Frontal variation history of Garibaldi Glacier from Landsat TM, ASTER and aerial photographs. The background is a 01/15/2011 ASTER image.

TCD
6, 3503–3538, 2012

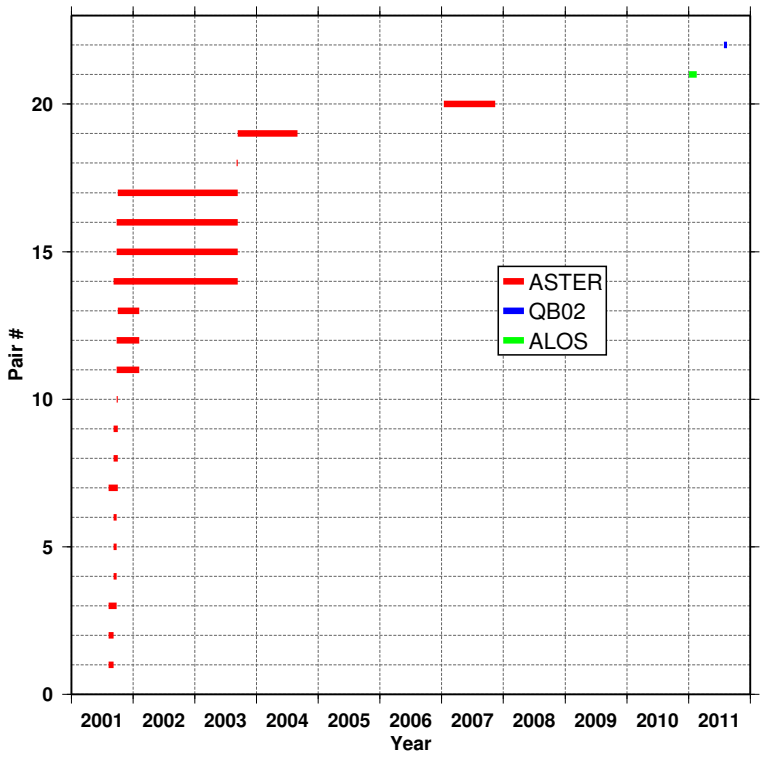

Fig. 8. Date intervals for 22 pairs that produce usable pixel-tracking results. The most recent is a QB02 pair (blue), the next most recent is an ALOS pair (green), and the remainder are ASTER pairs (red). These are from a total of 1 QB02 pair, 3 ALOS pairs and 119 ASTER pairs processed.

TCD
6, 3503–3538, 2012

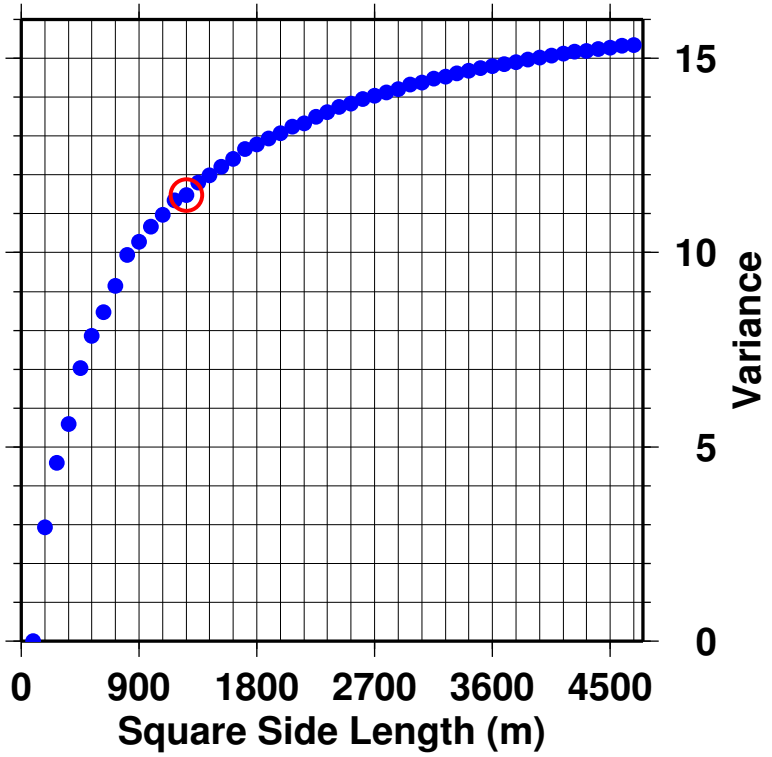

Fig. 9. A plot of pixel size (listed as side length of square pixel) vs. variance of bedrock $\frac{dh}{dt}$, plotted as blue dots. Red circle indicates selected "corner" point, 1260 m is selected as the area of maximum correlation for the $\frac{dh}{dt}$ variance.

TCD
6, 3503–3538, 2012

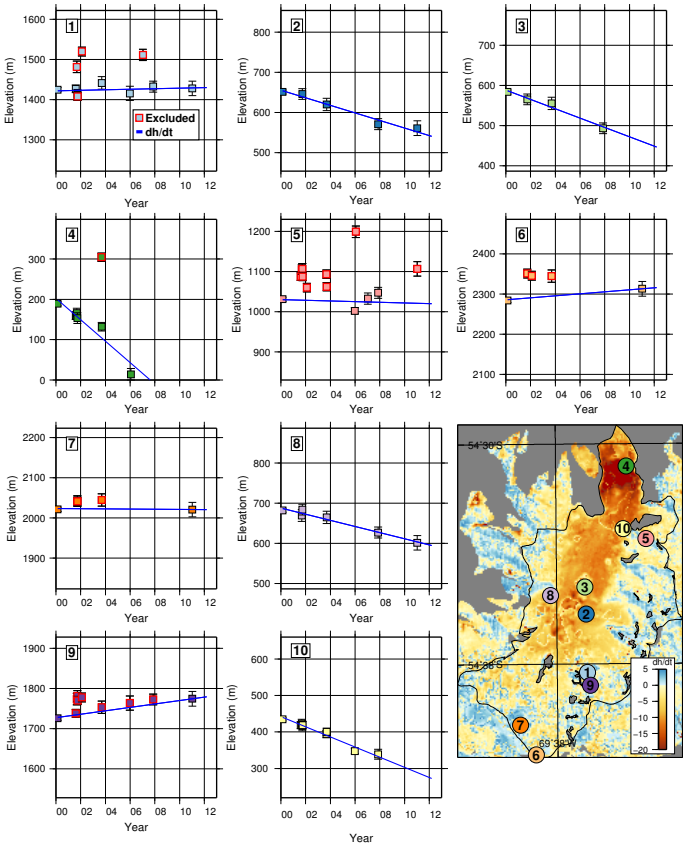

Fig. 10. Elevation values and $\frac{dh}{dt}$ for randomly selected pixels over Marinelli Glacier. The left-most elevation in each graph is the SRTM elevation at that pixel. Blue lines indicate the $\frac{dh}{dt}$ calculated for each pixel, elevation points bolded red are excluded from $\frac{dh}{dt}$ calculation. The bottom right panel shows the $\frac{dh}{dt}$ map, with numbered circles indicating the location corresponding to each graph.

TCD
6, 3503–3538, 2012

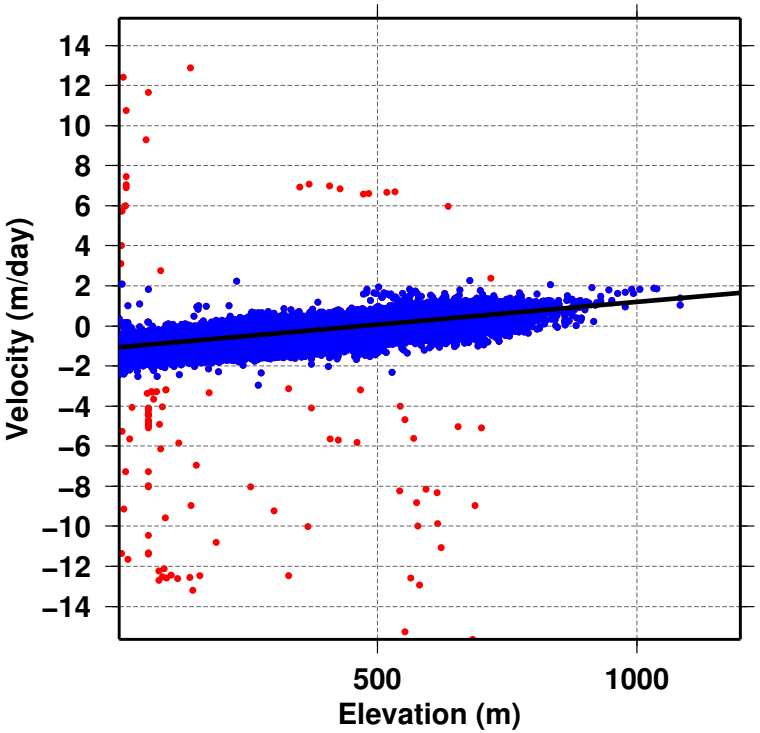

Fig. 11. Scatter plot of E–W "bedrock" velocities for the 09/07/2001 to 09/25/2001 ASTER pair. The black line shows the linear trend fitted to the blue points, this is removed from the overall E–W velocity results. Red points are excluded when fitting the trend (they are greater than $\pm\sigma$ from the median value). This cutoff makes a negligible difference in the trend for this pair, but for other pairs it can change the trend significantly (e.g. >1 m day^{-1} per 1000 m elevation).

TCD
6, 3503–3538, 2012

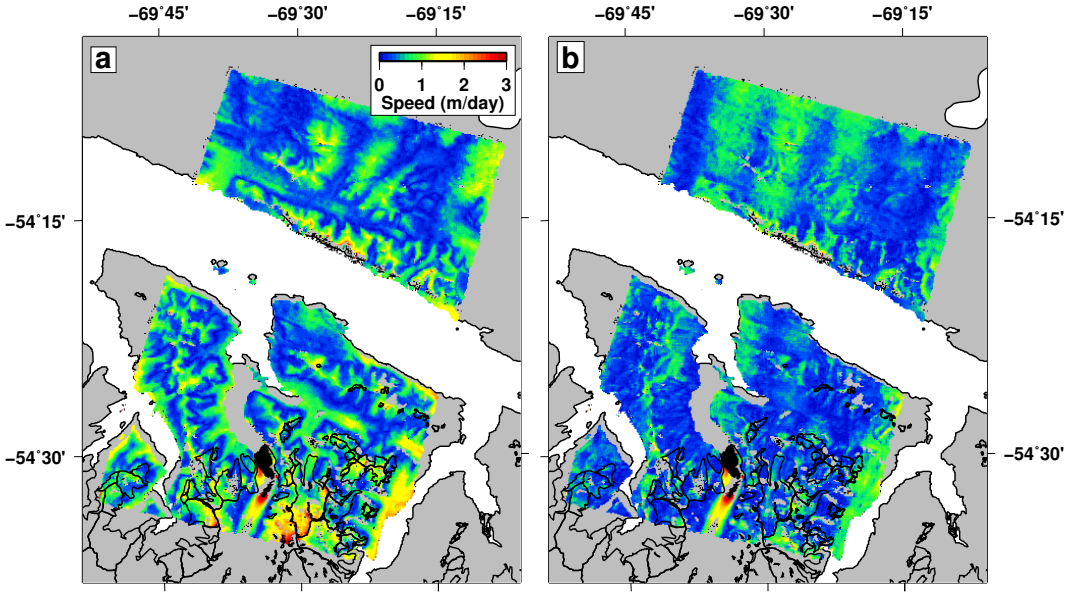

Fig. 12. Effect of elevation-dependent velocity correction for 09/07/2001 to 09/25/2001 ASTER image pair covering Marinelli Glacier. Glacier outlines in black, bedrock in gray (correction is not applied to water pixels). Panel **(a)** is a map of speeds with no correction applied, panel **(b)** is a map of speeds with correction applied. Correction significantly reduces bedrock motion, the mean and standard deviation for the entire pair drops from 0.6 ± 0.4 for the uncorrected speeds to 0.4 ± 0.3 for the corrected speeds.

TCD
6, 3503–3538, 2012